5. Effect of Heat Treatment on the Ballistic Performance of AA 7017 Alloy Plate against High Hardness Steel Core Projectiles

5.1. Introduction

This Chapter makes an attempt to evaluate the ballistic behavior of 40 mm thick AA 7017 alloy plates against high hardness steel core projectiles in different heat-treated conditions. This part of work also elucidates the effect of heat-treatment on the mechanical properties and impact toughness of the material as well as the overall effect of all these factors on ballistic performance of the material.

5.2. Results

5.2.1. DSC thermograms

The DSC thermograms for differently heat treated AA-7017 samples at a heating rate of 20°C/min are given in Fig 5.1. The DSC plots of UA and PA samples display three distinct regimes. They refer to an endothermic reaction region at lower temperature (regime I), an exothermic reaction doublet at an intermediate temperature (regime II) and an endothermic reaction at higher temperature (regime III). In contrast, the exothermic region is absent in the OA specimen. In addition, the temperature range of the region I is also shifted to higher temperature. Such a contrast brings out phases present under various heat treated conditions and their possible transformations.

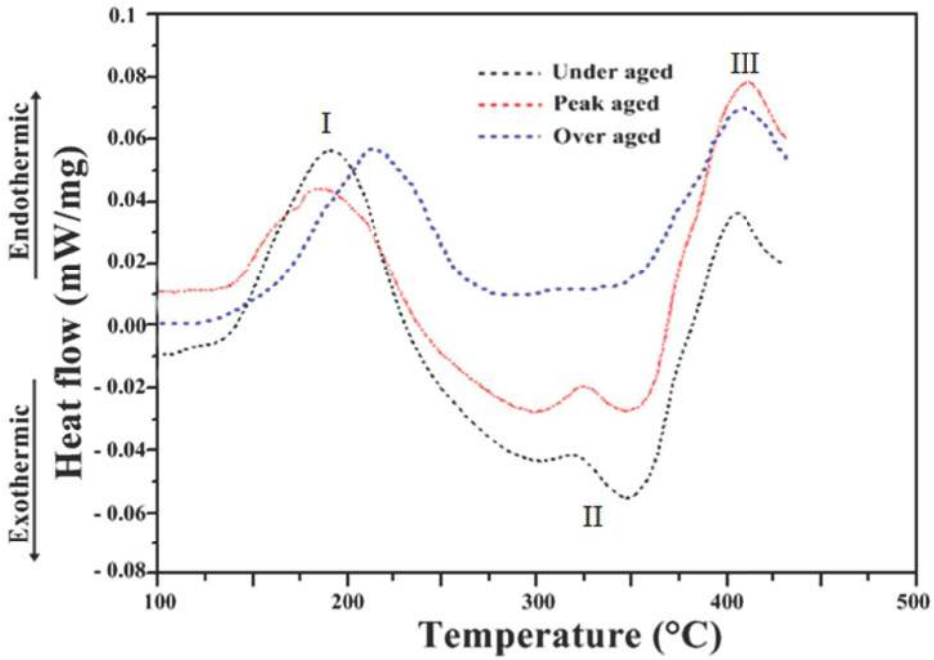

Fig 5.1: DSC thermograms of UA, PA and OA AA-7017 samples.

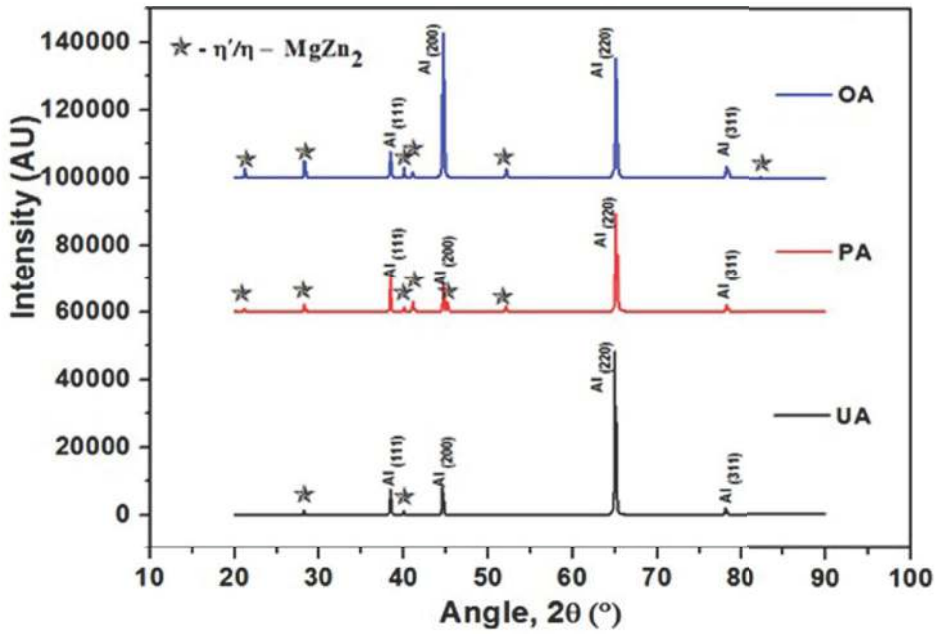

Fig. 5.2: X-ray diffractograms of UA, PA and OA AA-7017 samples.

5.2.2. X-ray Diffraction patterns

The X-ray diffractograms of AA-7017 alloy at different heat treatment conditions is exhibited in Fig 5.2. The XRD patterns of the heat treated plates illustrate a few small peaks from the η ($MgZn_2$) and η' ($MgZn_2$) phases in addition to α-Al. Peaks corresponding to η ($MgZn_2$) and η' ($MgZn_2$) phases are prominent in PA and OA plates.

5.2.3. Texture characterisation

The texture of the heat treated plates in terms of orientation distribution functions (ODF) are shown in Fig. 5.3(a-c). There is a variation in the overall texture intensity observed in the three planes. The maximum overall ODF intensities in UA, PA and OA plates are 9.5, 13.7 and 18.1, respectively. The major texture components for UA, PA and OA plates are {1 0 3}⟨3 3 1⟩ [f(g) =3.4], {0 1 12}⟨7 12 1⟩[f(g)=4.1], {0 1 12}⟨2 12 1⟩[f(g)=4.2], {2 0 3}⟨3 0 2⟩[f(g)=6.1], {0 0 1}⟨1 0 0⟩[f(g)= 1.7], {1 1 2}⟨1 3 2⟩[f(g)=6.0], {1 1 3}⟨0 3 1⟩[f(g)=7.7], {1 1 1}⟨0 1 1⟩ [f(g)=6.5], {1 1 4}⟨1 1 0⟩ [f(g)=5.0], {1 1 4}⟨0 4 1⟩ [f(g)=6.2], {1 1 1}⟨1 1 0⟩ [f(g)=6.6]; {103}⟨3 3 1⟩ [f(g)=2.1], {0 1 12}⟨10,12,1⟩ [f(g)=2.3], {0 1 1}⟨1 0 0⟩ [f(g)=3.9], {1 0 4}⟨4 0 1⟩ [f(g)=1.8], {1 1 15}⟨2 13 1⟩ [f(g)=3.0], {1 1 15}⟨6 9 1⟩ [f(g)=3.2], {2 2 5}⟨2 3 2⟩ [f(g)=3.2], {1 1 3}⟨1 1 0⟩ [f(g)=3.8], {4 4 1}⟨1 0 4⟩ [f(g)=4.8] and {0 0 1}⟨6 5 5⟩ [f(g)=10.4], {5 5 1}⟨1 1 0⟩ [f(g)=15.6]. The corresponding typical β fibers of the UA, OA and PA plates are exhibited in Fig. 5.4. The β fibre is very weak in UA plate, while inhomogeneous with high intensity between {168}⟨211⟩ and {011}⟨211⟩ locations in PA and OA plates.

5.2.4. Mechanical properties

The representative true stress-strain curves of the differently heat treated AA-7017 alloy plates are displayed in Fig. 5.5. The mechanical properties of the heat-treated plates are summarized in Table 5.1. The PA plate shows the highest hardness, σ_{YS} and σ_{UTS}, whereas the OA sample displays lowest hardness and strength values. The UA sample illustrates the highest value of ductility measured in terms of percentage to failure, followed by OA and PA plates.

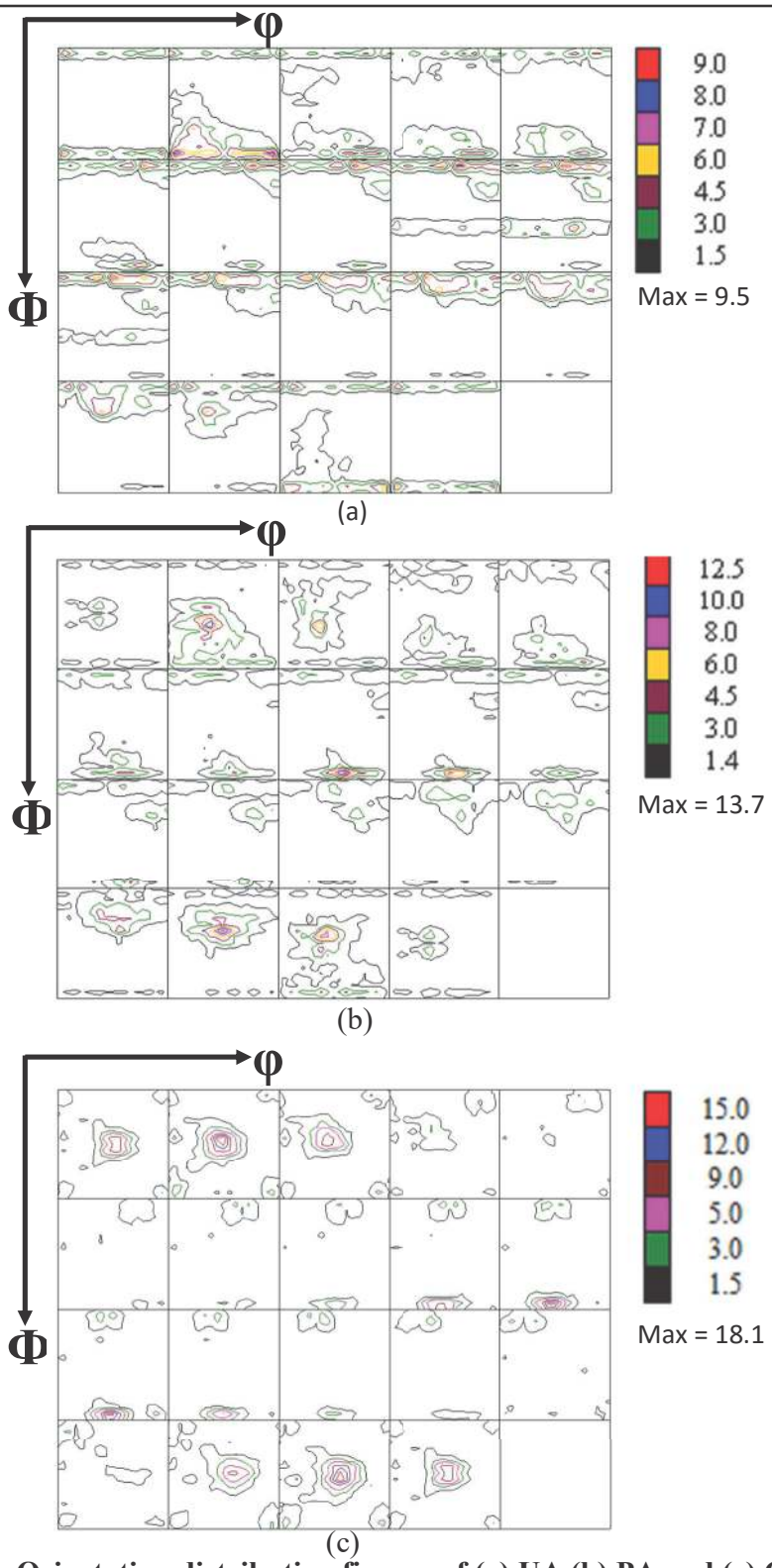

Fig 5.3: Orientation distribution figures of (a) UA (b) PA and (c) OA AA-7017 plates.

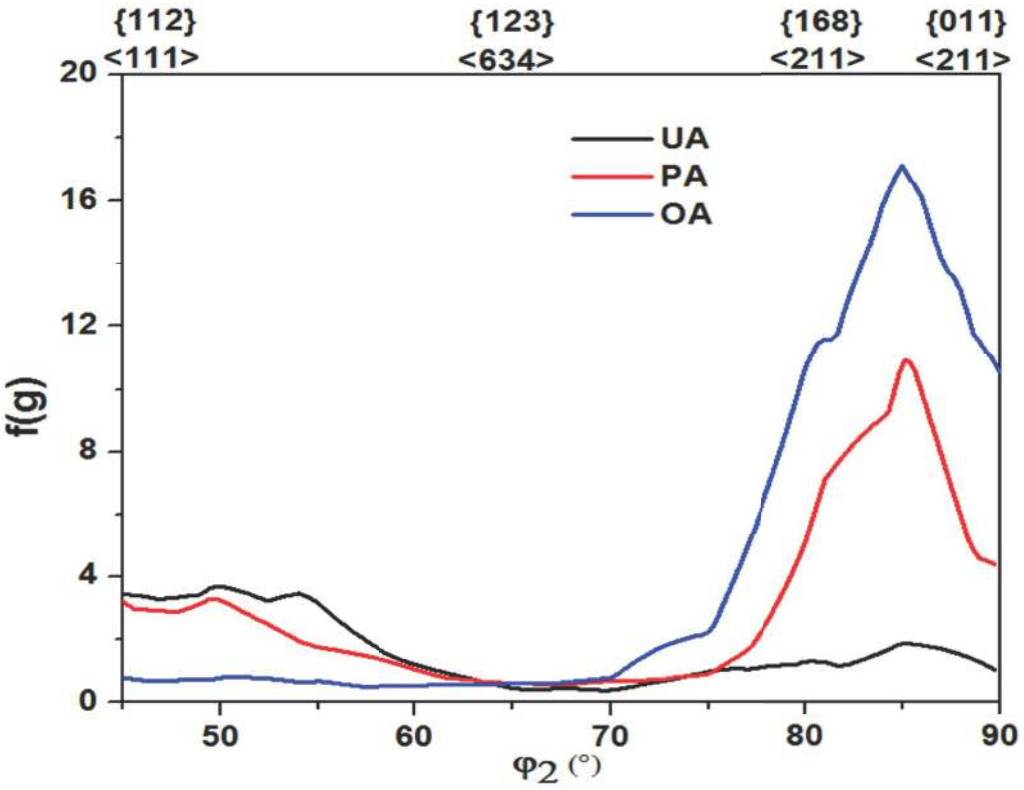

Fig 5.4: β fibres of UA,PA and OA AA-7017 samples.

The Charpy impact test results of UA, PA and OA plates are illustrated in Table 5.1. It can be noticed that UA and PA plates display the highest (17J) and lowest (9J) values of impact energy, respectively. The variations in fractographic features in the fracture surfaces of the broken Charpy impact specimens are depicted in Fig.5.6. The fracture surface of UA and OA samples are predominantly dominated by dimples. In PA samples, cleavage facets are observed along with dimples in the fracture surface.

5.2.5. Ballistic evaluation

The front and rear face of differently heat treated plates after ballistic tests are displayed in Fig. 5.7. The UA and OA plates fail to stop the projectiles. The projectiles have

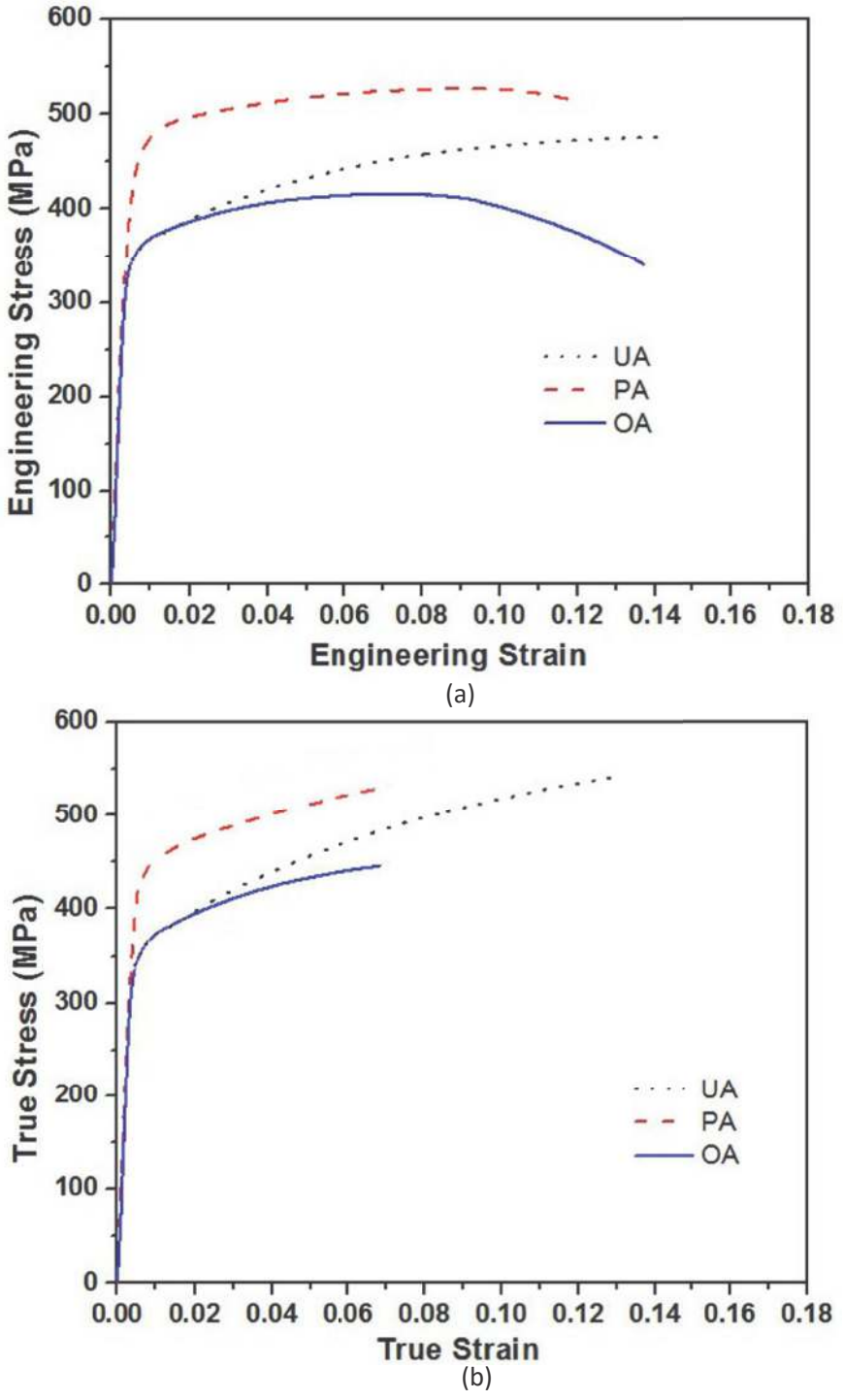

Fig. 5.5: (a) Engineering stress-strain and (b) True stress-strain curves of UA, PA and OA AA-7017 plates.

Table 5.1: Mechanical properties AA-7017 alloy in different heat-treated conditions

Heat treatment condition	YS (MPa)	UTS (MPa)	% Elongation	Hardness (HV)	CVN (J)
Under aged	345	484	13.7	139	17
Peak aged	437	513	11.4	160	9
Over aged	343	410	13.4	125	15

penetrated through the UA plates and the tip of the projectiles can be seen protruding out at the rear of the plates. There is a complete perforation observed in OA plates. In contrast, the PA plates are able to stop the projectiles successfully. The material flows out to form perfectpetalling damage pattern in the front side of the UA and OA target plates. On the other hand, spalling damage pattern is observed in the front face of PA plate. There is no bulging detected in the rear face of the PA plates.

5.3. Discussion

It is well known that the supersaturated solid solution (SSSS) of Al-Zn-Mg alloys produced by solution treated condition undergoes decomposition during aging and forms several second phase precipitates. The precipitation sequence is illustrated below (Stiller et al.,1999; Werenkiold et al.,2000; Buha et al., 2008):

Super saturation solid solution (SSSS) → Guiniere Preston (GP) zones → Semi-coherent η′ ($MgZn_2$) →Incoherent η ($MgZn_2$).

The precipitation sequence can be realised from the different regions of the DSC thermograms (Fig 1 (a)). It is to be noted that in precipitation hardenable aluminum alloys, precipitation and dissolution processes are exothermic and endothermic, respectively (Mukhopadhyay et al., 1987). The first endothermic region (region I) represents the dissolution of GP zones. The doublet observed in the exothermic reaction in region II is attributed to the separate sequential reactions involving η′ ($MgZn_2$) formation, dissolution of η′ ($MgZn_2$) and formation of η ($MgZn_2$) (Delasi and Adler, 1977). The higher temperature endotherm, region III illustrates the dissociation of η ($MgZn_2$) precipitates. Since the OA

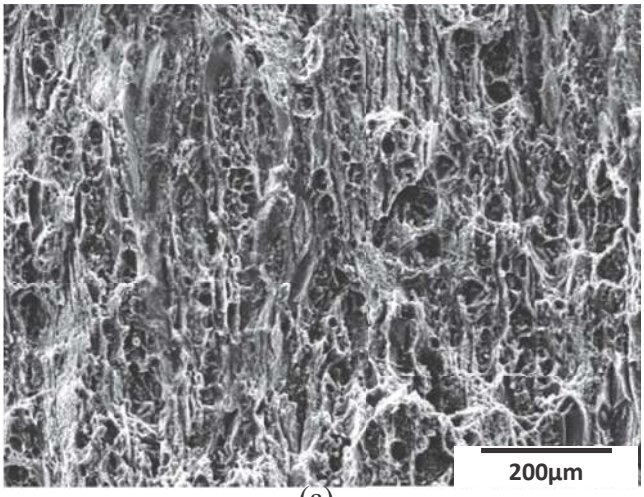

(a)

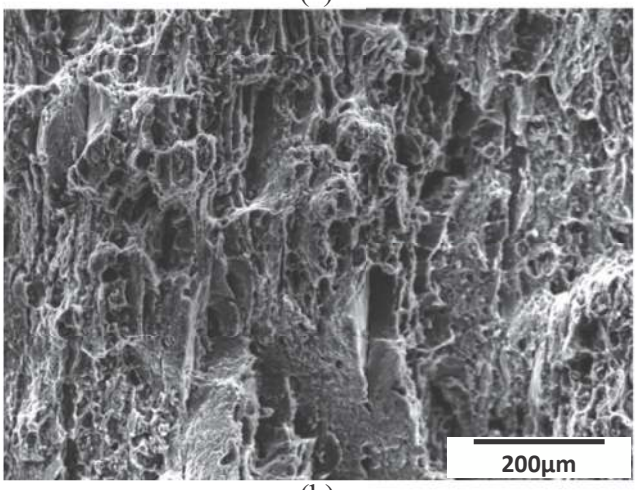

(b)

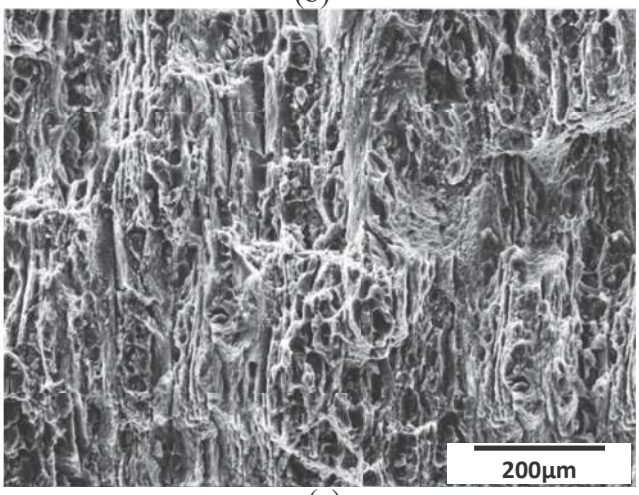

(c)

Fig. 5.6: Fractographs of the broken Charpy impact fracture surfaces of different heat-treated plates (a) UA (b) PA and (c) OA.

Fig. 5.7: Heat treated plates after ballistic impact (a) front face (b) rear face.

material contains η′ ($MgZn_2$) and η ($MgZn_2$) precipitates, the intermediate exothermic reaction (region II) is absent in its DSC thermograms. The shifting of peak of the endothermic reaction region I to higher temperature for OA material has been related to size of the η ($MgZn_2$) precipitates. The coarser η ($MgZn_2$) precipitates in OA plate reduces the solubility and hence increases the temperature of dissolution. It is to be noted that Rout et al. have reported that the size of the η ($MgZn_2$) precipitates increases from 35μm in PA to 90μm in OA plates of the AA-7017 alloy (Rout and Ghosh, 2012). The precipitation sequence and the peak temperatures of the differently aged specimens are in agreement with previously reported other 7000 series aluminium alloys (Delasi and Adler, 1977; Park and Ardell, 1989). Prominent peaks of η′ and η precipitates are also observed in the XRD diffraction pattern of PA and OA plates (Fig.1(b)). This reinforces the sequence of precipitation during aging as mentioned above.

From the texture measurements, it is observed that the overall intensity of ODF increases from UA to OA plates. The texture components observed in the UA plates are either recrystallisation components or components which are located near to these. A continuous fibre is also observed between φ=0° to 90° in φ2 = 0° section (Fig.2(a)). It appears that these components are moving towards typical cube texture during aging. However, the aging time and temperature of UA plate are not sufficient for complete recrystallization. The overall intensity is low in β fibre which is nearly homogeneous. The PA plate on the other hand display high intensity between {168}⟨211⟩ and {011}⟨211⟩ in β fibre and several other components with reasonable intensities. The continuous fibre between φ=0° to 90° in φ2 = 0° is broken. The texture is quite sharp and the main component is close to typical Bs component in OA plates. This corresponds to high intensity between {168}⟨211⟩ and {011}⟨211⟩ location in β fibre. The cube component further weakens. This clearly reflects that the texture of the hot rolled plates continuously changes from UA to OA plates.

Strength and hardness values display an increase and decrease from UA to PA and PA to OA plates, respectively (Table 5.1). Previous studies have also reported similar change in strength and hardness with aging (Dumont et al., 2003; Dumont et al., 2004). The

deviation in strength and hardness can be explained from the change in morphology of the precipitate phases. It has been reported that UA, PA and OA plates contain very fine and coherent (G.P.) zones, semi-coherent (η′) precipitate and non-coherent η precipitates, respectively (Rout and Ghosh, 2012; Dumont et al., 2003; Dumont et al., 2004; Mondal et al., 2011). In the UA condition, the G.P. zones produce local strains which impede the movement of dislocations and increase the strength. In PA condition, ordering of the larger clumps of η′ precipitates takes place which are semi-coherent to the matrix. The semi-coherent precipitates produce an increased strain field in the matrix and a further increase in the strength and hardness. With further aging the equilibrium phase is formed. These particles are no longer coherent with the matrix and therefore the hardness is lower in OA condition. The mechanical properties are in agreement with the precipitation sequence indicated by the DSC thermograms and XRD diffraction patterns (Fig. 5.1-5.2). As strength and ductility values are inversely proportional to each other, with high strength the PA plate displays lower ductility.

The impact energy variation can be explained from the appearance of fracture surfaces of the broken Charpy samples (Fig. 5.6). The variation in Charpy impact energy values can be corroborated with the change in morphology of the precipitate phases during heat treatment. The presence of dimple like morphology in the fracture surface of UA and OA plates indicates a ductile mode of failure consisting of void nucleation, growth and coalescence. This explains the observation of higher impact energy value of the UA and OA plates. In PA samples, the cleavage facets reduce the energy necessitate to fracture and hence decreases the Charpy impact energy. The cleavage facets are formed due to a combination low ductility and precipitate free zones along grain boundaries in PA condition.

Observation of spalling and petalling damage at the front face of PA and UA plates are very well in agreement with those of elongation and Charpy impact energy values. There are two material parameters namely, (i) hardness and (ii) impact toughness which are important for optimizing the ballistic performance. The projectile imparts its kinetic energy to the target plate on impact. The target plate absorbs the projectile's kinetic energy by plastic deformation. As a result, the material properties which prevents the plastic deformation, augments the ballistic resistance. In addition, increasing the hardness of the target plate

enhances the erosion as well as fracture of the projectile. This impairs the penetration capability of the projectile and results in lesser penetration. Higher toughness value facilitates the material to absorb impacted energy in a homogeneous manner. Therefore, material toughness also supplements to the ballistic resistance of the material. From the present study, it is observed that the PA plate exhibits higher ballistic resistance due to its superior strength and hardness values than those of the UA and OA plates. It is to be noted that the UA plates display highest ductility and Charpy impact values but they show inferior ballistic property in comparison to that of the PA plates. Thus, it appears that the material hardness is a leading factor in comparison to other mechanical properties to tailor the ballistic performance. This is in agreement with previous investigations (Dikshit et al., 1995;Übeyli et al., 2007;Borvik et al. 2009). It has already been mentioned that the presence of texture introduces a gradual non-uniform dissipation of energy during ballistic impact and impairs the ballistic resistance of the material. However, in the heat treated plates the variation of texture intensity is not very high. Hence, microstructural constituents are vital in deciding the mechanical properties and subsequently the ballistic performance of the heat treated plates.

Srivathsa and Ramakrishnan have developed an empirical model that defines a parameter called "ballistic performance index (BPI)". The ballistic performance of a metallic armour plate in this model is described in terms of mechanical properties of the materials and striking velocity of the projectile (Srivathsa and Ramakrishnan, 1997; Srivathsa and Ramakrishnan, 1998). The ballistic performance index (BPI) is a dimensionless quantity and is given in Eq. (5-1).

$$\mathbf{BPI} = \left[\frac{\alpha_I}{2(1+k_b)^2} + \alpha II\frac{(1+k_e)^2 k_\gamma^2}{2k_j^2} + \frac{1}{k_j}\left(1+\frac{1}{k_p}\right) + \frac{1}{2k_p^2} + \frac{1}{2}(1+\frac{1}{k_p})^2\right] \text{------ (5.1)}$$

The terms αI and αII are the fractional widths of the constrained and the unconstrained regions respectively during ballistic impact. The non-dimensional parameters ke, kp, kj, kb, and kn are computed using the following relations:

$$k_v = \sqrt{\frac{1-\nu}{(1-2\nu)(1+\nu)}} \qquad k_b = v_r\sqrt{\frac{\rho}{K}} \quad \text{where } k = \frac{E}{3(1-2\nu)}$$

$$k_e = \frac{v_r}{k_v}\sqrt{\frac{\rho}{E}} \qquad k_p = v_r\sqrt{\frac{\rho}{E_p}} \quad \text{where } E_p = \frac{\sigma_u(1+\varepsilon_r) - \sigma_y}{\varepsilon_r}$$

$$\alpha_I = 1 - \alpha_{II} = 1 - \sqrt{\frac{v_I}{v_0}}$$

$$v_I = \frac{-k_v\sqrt{\rho E} + \sqrt{k_v^2 E\rho + 10.4\rho\sigma_y}}{2\rho}$$

where ρ = density, E = The elastic modulus, σ_y = Yield strength, σ_u = Tensile strength, ν = Poisson's ration, ε_r = Reduction in area, v_0 = The striking velocity and v_r is= $v_0/1.85$. The BPI considers elastic deformation (first two terms), plastic deformation (third and fourth term) and kinetic energy imparted to the target material (fifth term) to assess the ballistic performance. The BPI is useful in deducing the ballistic performance of a wide range of armour materials with reasonably good accuracy. In the present study, the BPI of UA, PA and OA plates has been calculated using the mechanical properties data and these are plotted against aging conditions (Fig. 5.8). It is observed that the PA plates display the highest value of BPI which is also in agreement with the lowest value of DOP.

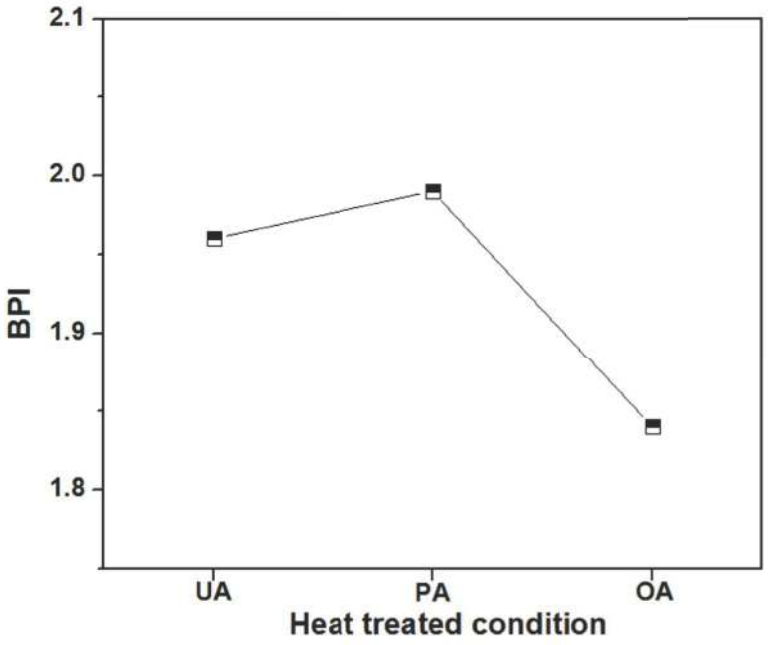

Fig. 5.8: Ballistic performance index (BPI) as a function of heat-treatment conditions. (The points are joined as a guide to the eye only)

5.4. Conclusions

The change in morphology of the precipitate phases during heat treatment has brought about a variation in strength and hardness of the different heat treated plates. The PA plates show highest strength and hardness due to a fine distribution of G.P. zones and η′ precipitates. Consequently, the PA plates demonstrate the best ballistic performance among the heat treated plated. As there is no significant variation in the overall texture intensity observed in the three different heat treated condition plates, the changes in microstructure play a dominant role in defining the mechanical properties and subsequently the ballistic behavior of AA-7017 alloy. Hence, the incorporation of microstructural observation and crystallographic texture gives a better understanding of the ballistic behavior of the material.